Effect of hydrogen-induced surface steps on the nanomechanical behavior of a CoCrFeMnNi high-entropy alloy revealed by in-situ electrochemical nanoindentation

Dong Wang [a], Xu Lu [a], Yun Deng [a,*], Di Wan [a], Zhiming Li [b,c], Afrooz Barnoush [a]

[a] Department of Mechanical and Industrial Engineering, Norwegian University of Science and Technology, Richard Birkelands vei 2B, N-7491, Trondheim, Norway

[b] Max-Planck-Institut für Eisenforschung, Max-Planck-Str. 1, 40237 Düsseldorf, Germany

[c] School of Materials Science and Engineering, Central South University, Changsha 410083, China

*corresponding author: Yun Deng; E-mail: dengyun967514@gmail.com

Abstract

The effect of hydrogen on the nanomechanical properties of CoCrFeMnNi high-entropy alloy was investigated by in-situ electrochemical nanoindentation testing. The changes in surface morphology, elastic modulus, pop-in load, and hardness during hydrogen ingress and egress processes were systematically evaluated. The results show that hydrogen charging leads to the formation of irreversible slip lines accumulated as surface steps. Furthermore, the irreversible reduced pop-in load and elastic modulus, and reversible increased hardness are detected. In this paper, the mechanisms of hydrogen-induced surface steps together with their further influences on the nanomechanical properties are discussed in detail.

Keywords:

In-situ electrochemical nanoindentation; High-entropy alloy; Hydrogen embrittlement; Hydrogen-induced surface steps; Electron channeling contrast imaging; Nanomechanics

1. Introduction

High-entropy alloys (HEAs) are substances that are comprised of five or more metallic elements with (near-) equal atomic ratio [1]. Since first introduced by Yeh et al. [2], HEAs have attracted considerable research attention because of their extraordinary mechanical properties such as the excellent combination of high strength and good ductility, high toughness, and good creep resistance [2-5]. All of these astonishing properties make HEAs a group of promising materials for turbine blades, nuclear constructions, liquid gas storage and transportation, and so forth [1, 6]. However, with the aforementioned potential applications, a hydrogen-rich service environment can lead to a high possibility of unexpected failure owing to hydrogen embrittlement, which is in accordance with the concept of hydrogen-induced degradation of metals with a transition from ductile to brittle failure [7, 8]. Therefore, the effects of hydrogen on the mechanical responses of HEAs should be investigated thoroughly prior to designing them for potential applications.

The mechanism of hydrogen embrittlement has been studied intensively but is still a controversial topic without a clear consensus. Different mechanisms have been proposed based on various experiments and observations, among which the hydrogen-enhanced decohesion (HEDE) [9, 10], hydrogen-enhanced localized plasticity (HELP) [7, 11, 12], adsorption-induced dislocation emission (AIDE) [13, 14], and "Defactant" [15-17] are the most popular models. The HEDE mechanism, proposed by Troiano et al. [9], postulates that the bonding energy between atoms is reduced by the presence of hydrogen and thus there is an increased risk of decohesion. The HEDE mechanism has been widely used to explain the cleavage-like failure and intergranular fracture surface in high strength steels [18, 19]. The HELP mechanism postulates that the mobility of dislocations is increased by the dissolved hydrogen due to the shielding effect on the elastic stress field of dislocations, thus resulting in slip localization and denser dislocation pile-ups [7, 11, 20]. The HELP mechanism was directly proven by the in-situ transmission electron microscopy (TEM) technique [12], where the enhanced dislocation motion was directly observed when hydrogen gas was introduced around a thin specimen subjected to plastic deformation. However, contradictory results have also been reported showing a hydrogen-restricted dislocation mobility effect [21, 22]. The AIDE mechanism, proposed by Lynch [13, 14], concludes that hydrogen-assisted cracking occurs because of the adsorption of hydrogen at crack tips. Specifically, the adsorbed hydrogen facilitates the emission of dislocations from crack tips and therefore promotes the occurrence of coalescence of cracks with voids to lower strains. The Defactant model, based on thermodynamic calculations, suggests that the formation energy of defects (such as dislocations and stacking faults) is reduced by the presence of defactant solutes, such as hydrogen [15-17]. It is necessary to mention here that hydrogen embrittlement is a complex process that depends heavily on the metals and applied environment and no aforementioned mechanisms can explain the phenomena exclusively. Moreover, these mechanisms are not completely distinct but share some overlaps with each other [23].

Among the various HEAs systems, CoCrFeMnNi alloy with five elements in equiatomic concentrations is the most appealing one owing to the thermodynamically stable single face-centered cubic (FCC) phase, the outstanding mechanical properties that provide a good combination of strength and ductility at room temperature [1, 24], and the superior fracture resistance at low temperatures [25]. Recently, the susceptibility of CoCrFeMnNi to hydrogen embrittlement has been reported with interesting conclusions. Luo et al. [26] reported results from in-situ tensile tests on electrochemically charged samples and the findings demonstrated that the dissolved hydrogen at relatively low concentrations (8.01-33.25 wppm) increases both the strength and ductility rather than causing catastrophic failure. They proposed that the charged hydrogen reduces the stacking fault energy and the phase stability. Therefore, the density of nano-twins is increased leading to an enhanced work hardening capability, and this thus enhances both the strength and ductility. Zhao et al. [27] charged the tensile test samples with 15 MPa gaseous hydrogen at 300°C for 72 h (76.5 wppm) and the results showed that the ductility reduction of the hydrogen-charged sample is only 5%. The fracture surfaces of charged and uncharged samples are similar, and both consist of dimples indicating ductile fractures. Also, Nygren et al. [28] performed tensile tests on samples charged by 120 MPa gaseous hydrogen at 200°C for 160 h with a much higher concentration (146.9 wppm) and the results showed that the CoCrFeMnNi alloy exhibites a significant reduction in ductility with the fracture mode changing from transgranular ductile failure to intergranular brittle failure. These macroscopic tensile tests on pre-charged samples provided useful information on the hydrogen embrittlement phenomena showing the changes in mechanical properties and fracture behavior with adequate dissolved hydrogen. However, due to the fact that HEAs exhibit high configurational entropy and low hydrogen diffusivity, disordered hydrogen distribution and strong hydrogen concentration gradient can be expected after the pre-charging. This makes it difficult to precisely connect the embrittlement phenomena with hydrogen concentration by using the conventional macroscopic tests with pre-charged samples. Moreover, the macroscopic tensile tests are not able to directly assess the small-scale interactions between hydrogen and dislocations, which is of strategic importance in understanding the hydrogen embrittlement mechanism. Therefore, it is necessary to perform investigations at nanoscale on the sample surface with constant and evenly distributed hydrogen to better understand the hydrogen effect on the degradation process. Recently, the effect of hydrogen on CoCrFeMnNi alloy was studied at nanoscale by Zhao et al. [29] by performing nanoindentation tests on pre-charged samples. They concluded that there is a hardness increment effect induced by the dissolved hydrogen because of the solid solution strengthening. However, owing to the outgassing diffusion process, a hydrogen depletion zone close to the surface could be expected in the pre-charged samples. This can result in uncertainties during nanomechanical testing, since the penetrating depth of the indenter is in the range of nanometers. Therefore, it is necessary to integrate in-situ hydrogen charging into nanoindentation testing to keep the surface hydrogen concentration constant by setting a proper electrochemical hydrogen charging process. The in-situ electrochemical nanoindentation (ECNI) technique, initiated by Barnoush et al. [30], has shown its advantage in probing the hydrogen effect on the nanomechanical properties of various metals [31-33]. By recording the high resolution load-displacement (L-D) data, both the mechanical properties, such as elastic modulus and hardness, and the discrete events, including dislocation nucleation, surface deformation, and phase transformation, are able to be detected [31, 34]. In this study, the in-situ ECNI tests were performed to obtain a better understanding of the effects of hydrogen absorption and desorption on the surface integrity and nanomechanical behavior of a CoCrFeMnNi HEA. With the applied in-situ technique, the drawbacks mentioned above from ex-situ charging tests can be avoided.

2. Experimental

2.1 Materials and sample preparation

The studied material is an equiatomic HEA with nominal composition $Co_{20}Cr_{20}Fe_{20}Mn_{20}Ni_{20}$ (at. %). The alloy ingot with dimensions of 25×60×65 mm^3 was cast in a vacuum induction furnace by using cleaned pure metals (purity higher than 99.8 wt%). Alloy sheets with dimensions of 10×25×60 mm^3 were further machined from the original cast block. The as-cast alloy sheets were hot-rolled at 900 °C to a 50% thickness reduction and then homogenized at 1200 °C for 2 h in an Ar atmosphere followed by water quenching. The detailed composition of the studied HEA obtained from chemical analysis is presented in Ref. [26]. The samples used for the in-situ ECNI tests were cut by electrical discharge machining into discs with a thickness of 2 mm and a diameter of 12 mm. The disc samples were ground sequentially by using 220-4000 grit SiC papers, followed by two polishing steps with 3 μm and 1 μm diamond sprays. The surface preparation was finalized by electropolishing in a methanol/H_2SO_4 solution at 35 V for 30 s. The surface quality was then checked by using the scanning probe microscopy (SPM), and the surface root-mean-square roughness was measured to be less than 0.2 nm over 100 μm^2. After surface preparation, the microstructure of the studied material was analyzed by using a high-resolution scanning electron microscope (SEM, Quanta 650 FEG, Thermo Fisher Scientific Inc.) with a backscattered electron (BSE) detector as well as the electron backscatter diffraction (EBSD) technique.

2.2 Electrochemical measurements

In order to determine the appropriate polarization potentials for the in-situ ECNI test, the polarization curve was measured by scanning from -2500 to 1500 mV with a scan rate of 1 mV/s. The electrolyte used in this study for both the polarization curve measurement and the in-situ nanoindentation test was a glycerol-based solution, which consisted of 600 g borax (sodium tetraborate decahydrate) dissolved in 1 L glycerol and diluted with 20% distilled water to ensure the conductivity [32]. In addition, 0.002 M $Na_2S_2O_3$ (sodium thiosulfate) was added into the solution to promote hydrogen absorption [35]. The developed electrolyte has an extremely low solubility and diffusivity of oxygen, and therefore, it is appropriate for preserving the sample surface from corrosion throughout the whole testing procedure [36]. A special three-electrode electrochemical cell was designed for the testing, and it consisted of a platinum counter electrode and a $Hg/HgSO_4$ reference electrode. All potentials in this study are reported versus this reference electrode.

2.3 In-situ ECNI

The in-situ ECNI test was performed with a Hysitron Tribo-indenter TI 950 equipped with a specially designed long-shaft Berkovich diamond tip, which was used not only for indenting but also for SPM imaging after each polarization condition to trace the changes of the surface integrity. The SPM images were analyzed with Gwyddion software. The load function used for the nanoindentation test starts with an 8000 μN/s loading segment until the peak load of 2000 μN plus a 0.45 s holding time, followed by an 8000 μN/s unloading segment with an additional 0.25 s holding time at 10% of the peak load for drift correction.

The sample was firstly tested in air as the reference condition, followed by the in-situ ECNI test at a sequence of -1500, -1600, and -1700 mV cathodic potential (CP) polarizations (more details are shown in the Section 3.2). After each cathodic polarization, an anodic polarization at 0 mV was performed to check the reversibility of nanomechanical properties after desorption of hydrogen. Hereafter, the cathodic charging potentials of -1500, -1600, and -1700 mV will be referred to as “CP1”, “CP2”, and “CP3”, while the corresponding anodic discharging potential of 0 mV will be described as “AP1”, “AP2”, and “AP3”, respectively. The sample was charged or discharged for 2 h at each potential before starting the first indentation test to ensure that a sufficient amount of hydrogen had been absorbed or desorbed. At least 27 indentations were performed in each condition to guarantee the reproducibility.

2.4 Electron channeling contrast imaging

The electron channeling contrast imaging (ECCI) technique has been proven to be an excellent SEM method based on the controlled diffraction condition with optimum contrast [37]. In the present study, ECCI was performed before and after the in-situ ECNI test to identify the evolution of dislocations induced by the electrochemical hydrogen charging. The imaging was performed at an acceleration voltage of 30 kV with a working distance of ~6.5 mm in the same SEM equipped with a solid-state four-quadrant BSE detector. The optimum channeling contrast was obtained by tilting the specimen to a situation where the grain matrix was exactly in the Bragg condition, thus enabling the diffraction vector in a two-beam condition. With the applied electron acceleration voltage and the activated diffraction condition, a visibility depth in the range of tens of nanometers was supposed to be reached [38].

2.5 Thermal desorption spectroscopy

In order to determine the content of absorbed hydrogen after different polarization process, the thermal desorption spectroscopy (TDS) test was carried out. The electrochemical hydrogen charging/discharging process was repeated on four samples that stopped at the end of each CP condition and AP3 condition, which together with an uncharged sample were tested by TDS. The TDS measurement was started immediately (less than one minute) after each charging and discharging process to eliminate the outgassing effect. The TDS was performed using a Bruker G4 PHOENIX DH hydrogen analyzer together with a mass spectrometry detector set up (ESD 100, InProcess Instruments, Germany), and the corresponding heating rate was 25 °C/min from 25 °C to 700 °C.

3. Results

3.1 Initial microstructure

Fig. 1 shows the BSE image and the normal direction-inverse pole figure (ND-IPF) map of the studied material, which revealed a single FCC structure consisting of grains with an equiaxed morphology and annealing twins. The average grain size was 160 μm, which was large enough to perform repeated indentation tests for all polarization conditions within a single grain to eliminate the influence of different orientations. In this study, the grain with a normal direction of <112> (parallel to the indentation direction) was chosen for the in-situ ECNI testing.

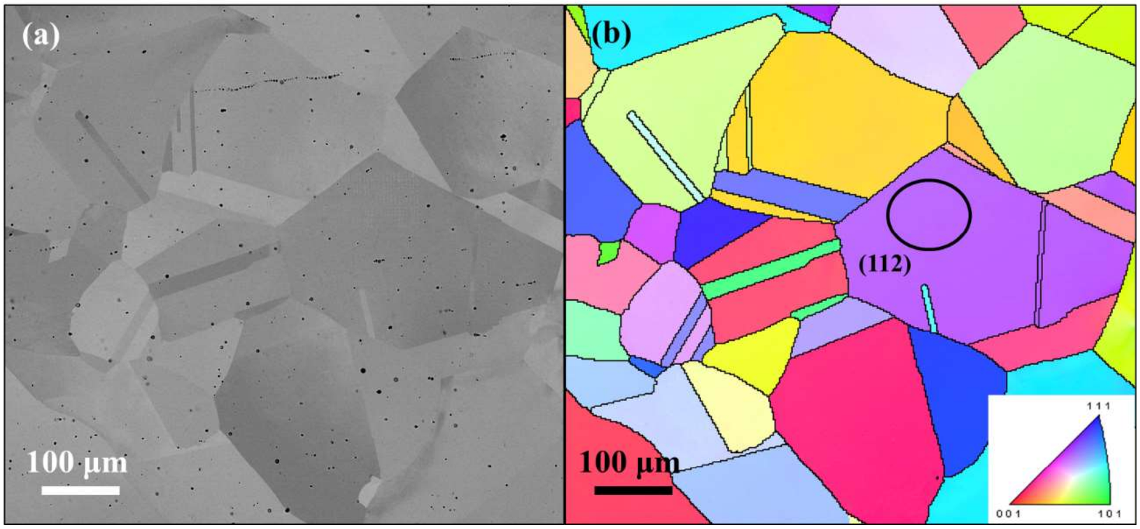

Fig. 1. (a) BSE image showing the microstructure of the investigated sample. (b) ND-IPF map of the same area with the marked (112) grain used for the in-situ ECNI testing.

3.2 Polarization curve

The polarization curve is shown in Fig. 2. The sample was cathodic polarized from -2500 to -1100 mV, where hydrogen was produced and diffused into the sample. A more negative cathodic potential resulted in a higher current density, which caused a higher hydrogen concentration on the sample surface. The anodic branch started at -1100 mV, and a passive region was obtained between -400 and 500 mV. As proposed in Section 2.3, in this study, -1500, -1600, and -1700 mV were chosen as cathodic charging potentials, while 0 mV, a value in the passive region, was chosen as the anodic discharging potential, at which the dissolved hydrogen diffused out; also, the sample surface could be kept free of corrosion. The chosen potentials are highlighted by horizontal dashed lines in the polarization curve shown in Fig. 2.

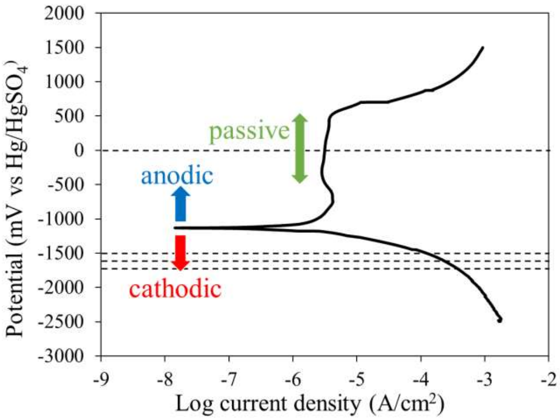

Fig. 2. Polarization curve of the investigated HEA sample. The horizontal dashed lines represent the chosen potentials for the in-situ ECNI tests.

3.3 The evolution of hydrogen induced surface steps (HISS)

The SPM images of the tested grain before and after the in-situ ECNI test under different conditions are exhibited in Fig. 3. Fig. 3a shows the original sample surface at air condition as the reference point. Figs. 3b-3d describe the sample surface after hydrogen charging at different cathodic potentials. The image in Fig. 3b was scanned after 2 h of hydrogen charging at CP1, and no noticeable changes on the surface can be seen. However, the evolution of surface steps on the sample surface can be easily observed after charging at higher potentials of CP2 and CP3 (Figs. 3c and 3d). It should be noted that the observed phenomenon (HISS) is a general feature for grains with different orientations in this material, and <112> grain is one of the most suited types of grains showing the slip behavior. By choosing <112> grain for testing, most slip features could be correctly revealed. Also, this relatively low-index orientation would not cause high complexity in the analysis. According to the corresponding surface roughness data shown in Fig. 3e, the root-mean-square roughness R_q before charging was 0.16 nm, and it remained the same after 2 h of CP1 charging followed by obvious increments to 0.26 and 0.28 nm at CP2 and CP3, respectively. The maximum height of roughness R_t showed a similar trend to that for R_q. Additionally, the ECC images of the sample surface before and after the whole in-situ ECNI test are presented in Fig. 4. The dislocations appeared as short white curved lines or dots on the dark background, indicating the intersections between the dislocations and the sample surface [38]. The fresh sample surface after electropolishing, as shown in Fig. 4a, contained uniformly distributed dislocations at a relatively low density, whereas the hydrogen-charged surface exhibited much more dislocations that were distributed mainly around the surface steps. Based on the ECCI results, the average dislocation spacing was measured as 0.5 µm for the fresh surface (Fig. 4a), while it decreased to 0.2 µm after whole charging/discharging polarizations (Fig. 4b).

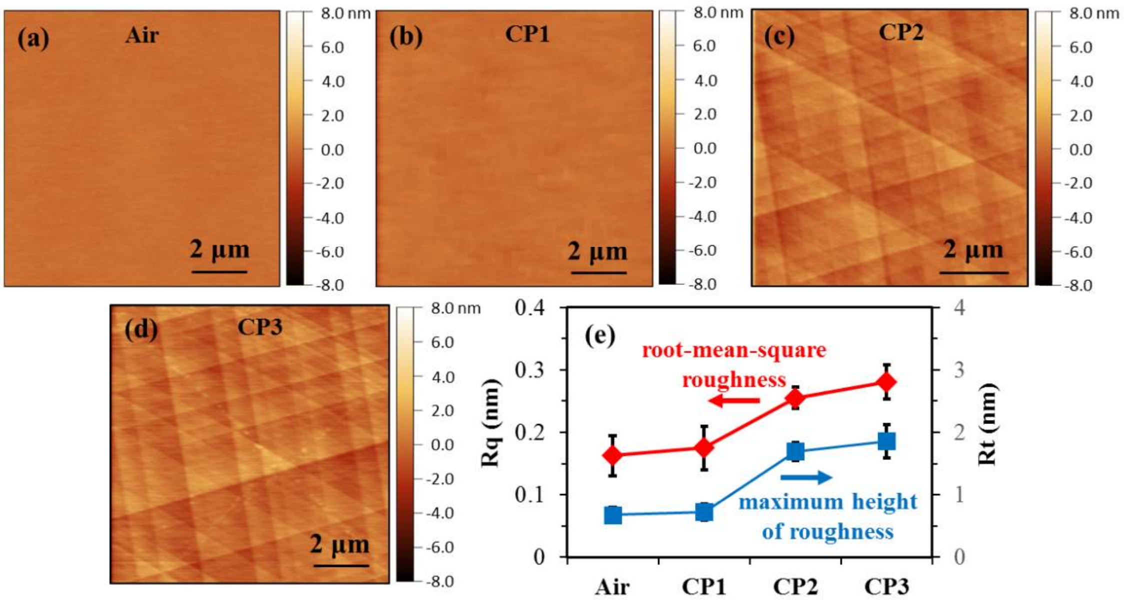

Fig. 3. The SPM images during in-situ electrochemical hydrogen charging: (a) before hydrogen charging in air; (b) after 2 h of hydrogen charging at CP1; (c) after 2 h of hydrogen charging at CP2; (d) after 2 h of hydrogen charging at CP3; (e) the root-mean-square roughness R_q (nm) and maximum height of roughness R_t (nm) under different electrochemical conditions.

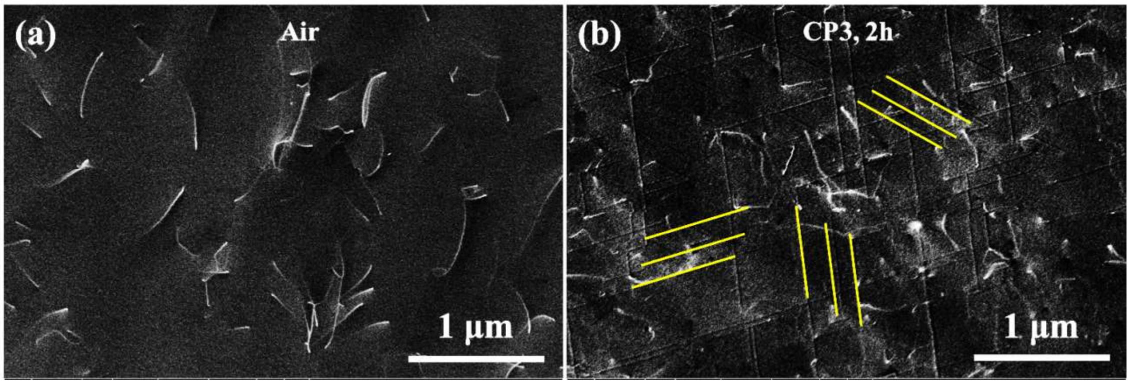

Fig. 4. The ECC images of the sample surface (a) in air and (b) after hydrogen charging at CP3 condition for 2 h. The yellow solid lines in (b) describe the directions of surface slip lines.

3.4 Nanomechanical properties

The representative L-D curves under different testing conditions are exhibited in Fig. 5. All of the curves clearly showed the following four stages: initial elastic loading; pop-in as a displacement burst; subsequent elastoplastic loading up to the maximum applied load; and elastic unloading. Except for the pop-in parts, the L-D curves measured in air and under APs were very similar, while evident changes were observed for all of the loading segments when polarized to CPs. In the following sections, the effects of hydrogen on each of the mentioned segments will be presented in detail.

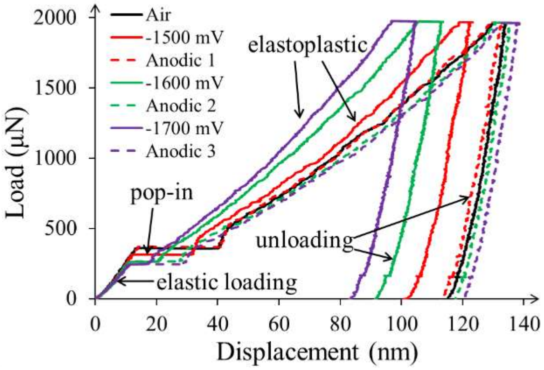

Fig. 5. The representative L-D curves for the tested grain in air, under three cathodic charging conditions and three anodic discharging conditions.

3.4.1 Elastic modulus

According to the Hertzian contact theory [39], the reduced modulus E_r of the sample can be obtained by fitting the initial elastic portion of the L-D curve with the relation:

$$P = \frac{4}{3} E_r \sqrt{R h^3} \tag{1}$$

where P is the applied load, h is the indentation depth, and R is the radius of the Berkovich tip curvature. Since the maximum penetration depth of the initial elastic segment is 10-15 nm, only the apex of the tip, which can be treated approximately as a sphere, is in contact with the material. The accurate R value was measured by performing indents on a standard fused quartz sample with a well-defined reduced modulus (69.6 GPa). By fitting the L-D curves with the Hertzian relation up to the depth of 15 nm, the Berkovich tip was found to be described perfectly as a sphere with a radius of 1.05 μm. Therefore, the E_r value of the tested sample can be determined by Eq. (1) and the Young's modulus E can be converted from E_r by:

$$\frac{1}{E_r} = \frac{1 - v_1^2}{E_1} + \frac{1 - v_2^2}{E_2} \tag{2}$$

where v is the Poisson's ratio. Here, the subscripts 1 and 2 represent the sample and the indenter tip, respectively. For a diamond tip, the elastic modulus is 1140 GPa, and the Poisson's ratio is 0.07. The Poisson's ratio of the studied CoCrFeMnNi alloy was reported as 0.26 [40]. Fig. 6 presents the Young's modulus E calculated by the Hertzian method under different conditions. The Young's modulus tested in air was 201.5 GPa, and there was no observable change (less than 1%) during the first CP-AP polarization sequence. However, when the applied potential was switched to CP2 and CP3, the Young's modulus was reduced to 197.0 and 184.4 GPa with 2.8% and 8.5% reductions, respectively, and no recovery was detected at the afterwards APs polarization.

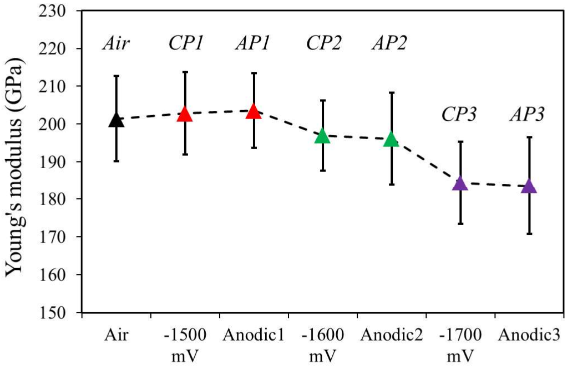

Fig. 6. Young's modulus of the studied CoCrFeMnNi HEA under different hydrogen absorption and desorption conditions.

3.4.2 Pop-in load

The pop-in phenomenon, as a sudden burst of indentation displacement, indicates the onset of plasticity. It has been proposed as a link to homogeneous dislocation nucleation or activation of a defect source such as dislocation, vacancy, or stacking fault [39, 41, 42]. Fig. 7a presents the magnified pop-in segments of typical L-D curves shown in Fig. 5. The observed changes in the pop-in load at different polarizations are summarized in Fig. 7b, where the mean values of the pop-in load with standard deviation error bars are presented. After the application of the first charging process at CP1, the pop-in load decreased from 352 μN (as obtained in air) to 328 μN. The reduced pop-in load then recovered to a similar value to that in air when AP1 polarization was applied. The reduction in the pop-in load at the following CPs scaled up with the values of applied potentials. However, in contrast to the AP1 polarization, the pop-in load showed no recovery effect at AP2 and AP3; instead, it remained at the same value as that for the previously applied CP2 and CP3 polarization, respectively.

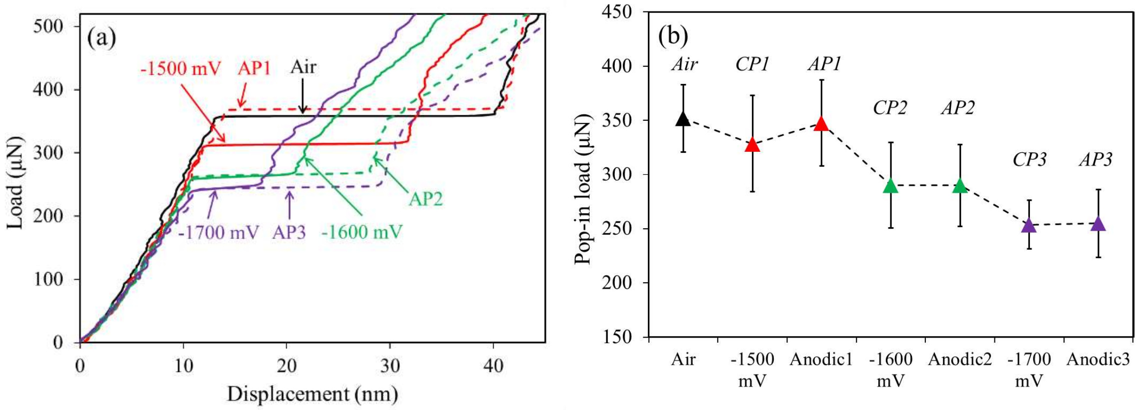

Fig. 7. (a) Magnified area of the initial elastic part and the pop-in part of L-D curves in Fig. 5. (b) The pop-in load under different polarization conditions.

3.4.3 Hardness

The hardness H of the studied material was determined from the elastic unloading segment of the L-D curve by using the Oliver-Pharr (O-P) method [43]:

$$H = \frac{P_{max}}{A_c} \tag{3}$$

where P_{max} is the maximum load during the nanoindentation test and A_c is the projected contact area according to the tip area function and the tip contact depth h_c, which can be calculated as shown in Eq. (4):

$$h_c \cong h_{max} - 0.75\frac{P_{max}}{S} \tag{4}$$

Here, h_{max} is the maximum displacement during the test and S is the stiffness extracted from the initial unloading slope of the L-D curve. The mean values of hardness under sequentially changed polarization conditions are shown in Fig. 8a. The hardness value in air was 3.36 GPa, and it accumulatively increased by 12.1%, 38.8%, and 54.8% at the applied cathodic polarizations of CP1, CP2, and CP3, respectively. In contrast to the irreversible behavior of the pop-in load and elastic modulus, the hardness recovered to (even slightly lower than) the original air-level at each AP polarization. The hydrogen-enhanced hardening effect can also be demonstrated by the reduced indenting contact areas under hydrogen charging conditions from the ECC images. As shown in Figs. 8b-8h, the radius of contact area in air was 0.66 nm, which was reduced to 0.61, 0.51, and 0.47 nm at CP1, CP2, and CP3 charging conditions, respectively. Furthermore, a fully recovered behavior of contact area was observed at each corresponding AP conditions.

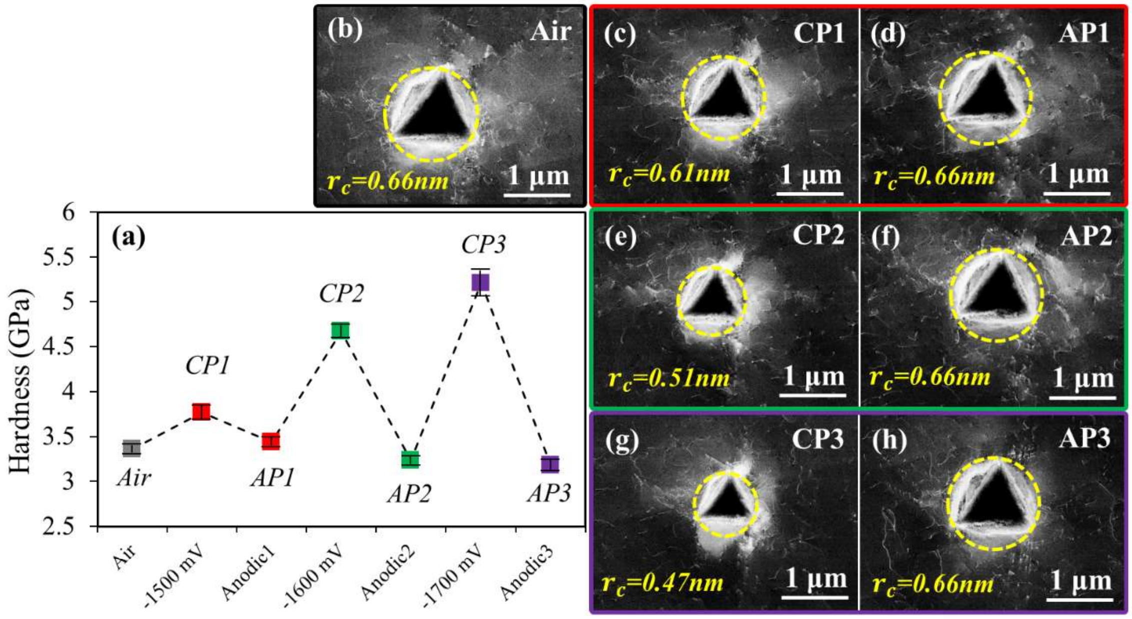

Fig. 8. (a) The mean hardness of the studied CoCrFeMnNi HEA under sequentially changed polarization conditions. (b)-(h) The ECC images of indents in different testing conditions with marked contact area.

3.5 Hydrogen content

The contents of hydrogen at different selected charging/discharging conditions were measured by TDS. As shown in Table 1, the amount of hydrogen in the uncharged sample is 0.0001 wppm, which increases to 0.10556, 1.15565, and 3.00399 wppm at the following CP1, CP2, and CP3 hydrogen charging conditions, respectively. After the 2 h anodic discharging process at AP3, the remained hydrogen content is 0.02980 wppm. According to the method used by Pontini and Hermida [44], the hydrogen concentration near the sample surface C_s during hydrogen charging can be estimated as follows:

$$C_s = \frac{\omega C_M}{4}\sqrt{\frac{\pi}{Dt}} \tag{5}$$

where ω is the thickness of tested sample, C_M is the dissolved hydrogen content measured by TDS, t is the hydrogen charging time, and D is the hydrogen diffusion coefficient chosen as 3.2×10^{-16} m^2/s from the austenitic stainless steel with similar crystal structure and composition [45]. Therefore, the hydrogen concentration $C(x,t)$ after charging time of t and at the depth of x can be calculated from the Fick's law-based "semi-infinite" model [45]:

$$\frac{C(x,t) - C_0}{C_s - C_0} = 1 - \mathrm{erf}\left(\frac{x}{\sqrt{4Dt}}\right) \tag{6}$$

$$\mathrm{erf}\,(u) = \frac{2}{\sqrt{\pi}}\int_0^u \exp\,(-u^2)du \tag{7}$$

where C_0 is the original dissolved hydrogen measured as 0.0001 wppm in air condition. The concentration profile of hydrogen as a function of depth at different CP conditions is shown in Fig. 9. It shows that after 2 h of cathodic charging at each potential, the hydrogen mainly distributed in the surface area within a depth of 5 μm. As summarized in Table 1, the hydrogen contents on the surface, which primarily affects the nanomechanical properties, are calculated as 31.43, 560.03, and 920.79 wppm after charging at CP1, CP2, and CP3, respectively.

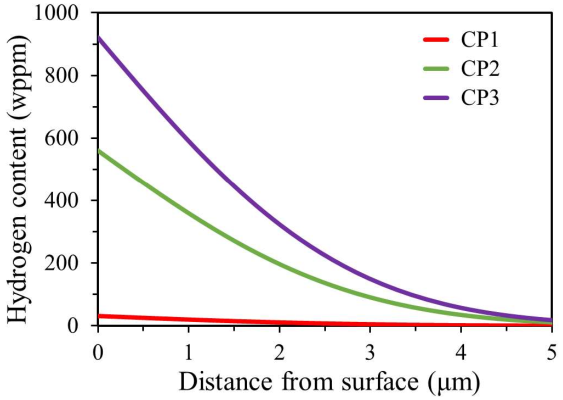

Fig. 9. Hydrogen distribution as a function of depth at different hydrogen charging conditions.

Table 1

Summary of the TDS results on samples in selected electrochemical polarization conditions.

Charging condition	Hydrogen content (wppm)	Sample thickness (mm)	Surface hydrogen content (wppm)
Air	0.00010	0.85	—
CP1	0.10556	1.02	31.43
CP2	1.15565	1.66	560.03
CP3	3.00399	1.05	920.79
AP3	0.02980	0.92	—

4. Discussion

4.1 Hydrogen induced surface steps (HISS)

As shown in Figs. 3 and 4, the formation of slip lines accumulated as steps on the sample surface with an increased dislocation density was observed after hydrogen charging process at CP2. It is necessary to mention that special care was taken during the installation of the sample into the electrochemical cell and there were no external forces applied to the surface during the charging process. Moreover, the SPM images of the sample surface after indenting in each charging conditions are shown in Fig. 10. Through comparing Fig. 10 and Fig. 3, it shows a negligible influence on the matrix topography by the indentation tests. This further confirms that the formation of surface steps was caused by the charging process instead of nanomechanical loading. Further, it can be deduced that the potential threshold for triggering the formation of HISS is somewhere between CP1 and CP2, i.e., between -1500 mV and -1600 mV.

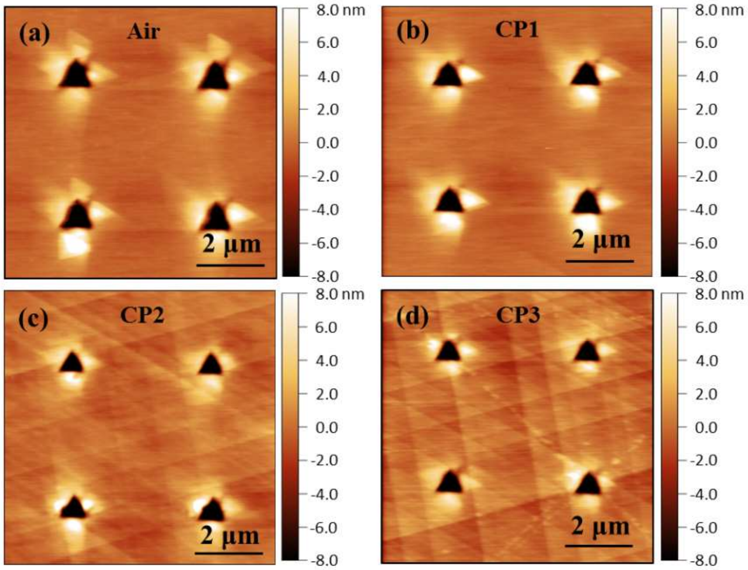

Fig. 10. The SPM images after indenting in each hydrogen charging conditions: (a) air; (b) CP1; (c) CP2; (d) CP3.

It has been reported that hydrogen can increase the mobility of dislocations because of the shielding effect on the interaction between dislocations and elastic obstacles in the frame of the HELP mechanism [7, 12, 46]. However, the hydrogen-enhanced dislocation mobility is not a sufficient condition for the formation of large number of surface steps with dislocations in this study. This is because the density of pre-existing dislocation in our sample was very low after the annealing process (Fig. 4a), which made it insufficient to form the dislocation structure as shown in Fig. 4b. Therefore, the multiple dislocations around surface steps appeared after CP2 condition must be newly generated. Base on the hydrogen concentration curve shown in Fig. 9, the atomic ratio between hydrogen and metal ${}^{H_a}/{}_{M_a}$ near the sample surface at CP2 condition can be calculated by:

$$ {}^{H_a}/{}_{M_a} = \frac{C_s \times {}^{N_A}/{}_{M_H}}{(10^6 - C_s) \times {}^{N_A}/{}_{M_A}} \tag{8} $$

where C_s is the hydrogen content on the surface layer in wppm as proposed in Eq. (5), N_A is the Avogadro constant, M_H and M_A are the molar mass of hydrogen and the studied equiatomic HEA, respectively. The SPM images in Fig. 3 show surface slip line formation at CP2 charging condition, which indicates that enough hydrogen is dissolved in the surface area to trigger the dislocation nucleation. The ${}^{H_a}/{}_{M_a}$ atomic ratio in the surface area at CP2 condition is calculated as 0.031 from Eq. (8). The correlation between the content of dissolved hydrogen and resulted lattice expansion can be described by the linear relationship [47]:

$$ \frac{\Delta V}{V_0} = \frac{H_a}{M_a}\frac{\Delta v}{\Omega} \tag{9} $$

Where ${}^{\Delta V}/{}_{V_0}$ is the change of lattice volume, Δv is the volume change of unit cell with one dissolved hydrogen atom, and Ω is the mean volume of metallic atom. The ratio of ${}^{\Delta v}/{}_{\Omega}$ was reported as 0.19 for 310 stainless steel [48], which has a similar crystal structure and composition to the studied material. Therefore, the lattice expansion due to hydrogen charging at CP2 condition is estimated as 0.59%. For simplicity, we assume that the lattice expansion is caused by isotropic internal stress due to abundant dissolved hydrogen. The internal stress σ_i can be estimated by using the proposed bulk modulus ($B = 137\ GPa$) from the same material as follow [49]:

$$ \sigma_i = B \cdot \frac{\Delta V}{V_0} \tag{10} $$

The internal stress in the surface area at CP2 condition is calculated as 808.3 MPa, which is about four times higher than the proposed yield stress [50]. Moreover, after the same calculation, the internal stress in the surface area at CP1 condition is only 45.9 MPa. Thus, the proposed mechanism can explain the formation of slip lines in the aspect of plastic deformation theory. It needs to mention here that the above estimation of the internal stress is based on the Hook's law and can only be regarded as an approximation. Nevertheless, the estimated stresses, though not precise, are able to qualitatively and comparably explain the plastic deformation with the occurrence of slip lines on the sample surface after CP2 polarization. Moreover, according to the Defactant model proposed by Kirchheim [15, 16], the dissolved hydrogen can act as defactants and reduce the formation energy of dislocations by reducing the dislocation line energy. As a result, the nucleation of dislocation is promoted by the dissolved hydrogen. Therefore, the combination of hydrogen-induced internal stress and the intrinsic hydrogen effect on reducing the dislocation formation energy is suggested as the reason for dislocation nucleation, followed by dislocations gliding to the surface and forming HISS due to the accumulation of slip lines. It is worth noting that such HISS phenomenon is uncommon for other conventional austenitic alloys. This is due to the combined intrinsic features of the studied CoCrFeMnNi HEA, including a low hydrogen diffusion coefficient [1], a low critical resolved shear stress [50], and a low stacking fault energy [51]. The low hydrogen diffusivity causes superabundant accumulation of hydrogen at the near-surface region, which results in a high internal stress. The low critical resolved shear stress makes the onset of planar dislocation slip easier under the hydrogen enhanced internal stress. The low stacking fault energy ensures the dislocations moving on certain preferred slip planes instead of cross-slipping or climbing, and therefore resulting in observable surface steps.

4.2 Effects of hydrogen and HISS on the nanomechanical properties

4.2.1 Effect of HISS on the elastic modulus

In general, the influence of hydrogen on the elastic modulus is still under debate. Tomatsu et al. [52] proposed that hydrogen charging has no effect on the elastic properties by performing in-situ ECNI tests on Ni-Cr bi-alloys. Shalskyi et al. [53] measured the time of passage of elastic waves in material with electrolytically absorbed hydrogen and found out the elastic modulus is enhanced by hydrogen. In contrast, Lunarska et al. [54] charged gaseous hydrogen into pure iron and found a decrease in elastic modulus by using the inverted torsion pendulum method within the temperature range of 100 to 200 K. In the present study, the elastic modulus was not affected by the hydrogen absorption-desorption processes at CP1-AP1 polarization, whereas noticeable reduction was observed when polarized to CP2 and CP3. However, if we interpret the reduction of modulus at CPs as a result of the dissolved hydrogen, the non-recovered value at the following APs after the desorption of hydrogen is unexplainable. Jiang et al. [55] performed nanoindentation tests together with theoretical calculations to study the effect of surface morphology on the nanomechanical properties, and the results indicated that the surface roughness significantly influences the elastic modulus. This is due to the fact that the elastic modulus in the current study was determined by fitting the initial elastic loading part of the L-D curve with the Hertzian contact model, and the maximum depth of elastic deformation is approximately 10-15 nm. By contrast, the hardness value was calculated by using the Oliver-Pharr method from the elastic unloading segment, which has a larger depth of approximately 85-120 nm. Therefore, due to the different effective depths between elastic modulus and hardness, the enhanced surface roughness is supposed to have a greater effect on the elastic modulus than on the hardness (cf. Fig. 6 and Fig. 8). As a significant hydrogen-induced surface topography change was observed in the present study (cf. Fig. 3 and Fig. 4), the hydrogen effect on the elastic modulus was not able to be directly detected and the reduction of the elastic modulus was mainly stemmed from the HISS.

4.2.2 Effect of HISS on the pop-in load

For the first sequence of charging and discharging (CP1 and AP1), the results revealed that there were no changes in the surface roughness (Fig. 3e). The average spacing of dislocations for the original sample was measures as 0.5 μm based on the ECCI result (Fig. 4a). As shown in Fig. 7a, the elastic region probed a maximum depth of 15 nm before the occurrence of the pop-in, thus indicating that the average dislocation spacing was ~33 times larger than the indented depth when the pop-in happened. Therefore, an indent placed randomly on the surface has a high probability of probing on an area without pre-existing dislocations. The absence of pre-existing dislocations implies that the pop-in phenomena indicate the homogeneous dislocation nucleation. The pop-in phenomena occur when the maximum shear stress τ_{max} reaches the theoretical critical shear stress, followed by subsequent dislocation gliding and other motion events [31, 39]. According to the continuum mechanics, the τ_{max} during the indentation testing occurs below the tip as follows [56]:

$$\tau_{max} = 0.31\left(\frac{6E_r^2}{\pi^3 R^2} P_{pop-in}\right)^{\frac{1}{3}} \tag{11}$$

Where P_{pop-in} is the pop-in load, E_r and R are the reduced modulus and tip radius, respectively, as proposed in Eq. (1). The τ_{max} values calculated in air, CP1, and AP1 were 4.06, 3.99, and 4.14 GPa, respectively. The shear modulus μ was calculated as 72.1 GPa based on the Young's modulus and Poisson's ratio. Therefore, the τ_{max} values in the aforementioned conditions are approximately equal to $\frac{\mu}{18}$, which is in good agreement with the Frenkel model for prediction of homogeneous dislocation nucleation [57].

The classic dislocation theory proposed the required free energy ΔG for nucleating a circular dislocation with radius r as [58]

$$\Delta G = 2\pi r W_{dis} + \pi r^2 \gamma - \pi r^2 b \tau_{max} \tag{12}$$

Here, W_{dis} is the dislocation line energy, γ represents the stacking fault energy and b is the Burgers vector (0.255 nm for the present HEA). Based on the Defactant model [15, 16, 59], the dissolved hydrogen can be assumed as defactants that reduce the formation energy of defects. For a linear dislocation, the dissolved hydrogen atoms can segregate around the dislocation and effectively increase the dislocation core radius and therefore reduces the dislocation line energy [60, 61]. Moreover, the stacking fault energy is also reduced by hydrogen, which has been illustrated via both experimental works and numerical simulations [62, 63]. Therefore, at the CP1 polarization with a uniform surface integrity, the reduction of pop-in load can be concluded as being caused by the hydrogen-enhanced homogeneous dislocation nucleation through the reduction of dislocation line energy and stacking fault energy.

For the following two cathodic charging processes with higher potentials at CP2 and CP3, the pop-in load decreased to 290 and 254 μN, with reductions of 17.6% and 27.8%, respectively, compared to air-values. The pop-in load remained the same at the following anodic polarizations when the dissolved hydrogen had diffused out of the sample surface. This is contradictory to the results in former in-situ ECNI studies [61, 64], which showed reversible behavior of the pop-in load during anodic polarization. However, in those former studies, the surfaces were reported to have no roughness change during the whole test. This means that the observed pop-ins are related to dislocation nucleation on a relatively dislocation-free area and the changes in pop-in load are not due to surface changes, but the ingression of hydrogen atoms. In contrast, the surface roughness in the present study increased with HISS formation at CP2 and CP3. It has been proposed that the surface steps strongly decrease the first dislocation emission, i.e. pop-in, by the stress concentration due to the decrease in initial contact area between surface steps and the indenter tip [65]. Another possibility is that hydrogen charging introduces multiple dislocations in the near-surface region, and the pop-in phenomenon begins at lower stress by activating the pre-existing dislocations instead of nucleating new sources [66]. Therefore, the pop-in behavior is very sensitive to the surface quality: for a defect-free surface, the pop-in is facilitated through the homogeneous dislocation nucleation, and reversible pop-in behavior with hydrogen ingress and egress can be observed. In other cases, the pop-in happens by activating the existing defects. In this study, the pop-in load at the CP1 condition was caused by the homogeneous dislocation nucleation with a reversible behavior. On the contrary, irreversible pop-in load reduction was observed at higher CPs due to the activation of the pre-existing dislocations by the concentrated stress.

4.2.3 Effect of hydrogen on the hardness

In contrast to the anodic non-recovery behavior of elastic modulus and pop-in load, the hardness showed a full recovery behavior at anodic conditions as shown in Fig. 8a. The hardness values at AP2 and AP3 were even slightly lower than that of uncharged sample. This softening effect has been reported as the result of formation of superabundant vacancies during hydrogen charging [29]. In this study, since the hardness values were extracted from the deeper unloading segment, it is suggested that the increment of hardness at CPs was not caused by the HISS but by the dissolved hydrogen in the affected area. To describe the dependency of hardness on the dissolved hydrogen, the elastoplastic regions of L-D curves can be represented by the Tabor relation-based Nix-Gao model [67]. Based on the Tabor's relation $H_0 = C\sigma$, the elastoplastic part can be expressed as follows:

$$P = H_0 A_c = C\sigma A_c \tag{13}$$

where P is the applied load and A_c is the projected contact area as proposed in Eq. (1). H_0 is the depth-dependent hardness during the elastoplastic regime, σ is the flow stress, and C is the Tabor factor as 3. In the current study, all the indents were performed on a defined coarse grain, which can be treated as a single crystal. Therefore, the hardening mechanisms caused by grain boundaries and phase boundaries are not considered. Hence, the flow stress σ is consisted of lattice friction (σ_{Fric}) and Taylor stress (σ_{Taylor}). The σ_{Fric} was proposed by Refs. [50, 68] as 190 MPa including the effect of solid solution hardening for the similar HEA, while the σ_{Taylor}, indicating the interaction between dislocations, is defined by Eq. (14) [67]:

$$\sigma_{Taylor} = M\alpha\mu b\sqrt{\rho_{SSD} + \rho_{GND}} \tag{14}$$

Here, M is equal to 3.06 as the Taylor factor, μ is the shear modulus, b is the Burgers vector, and α is an empirical factor related to the mean dislocation strength, which is chosen as 0.5 [31, 69]. The ρ_{SSD} and ρ_{GND} are the density of statistically stored dislocation (SSD) and geometrically necessary dislocation (GND), respectively. The ρ_{SSD} value is assumed as 5×10^{12} m^{-2} for an annealed sample, which matches perfectly with the estimated dislocation density from ECC image shown in Fig. 4a. Based on the ECCI result in Fig. 4b, the ρ_{SSD} value for the specimen after hydrogen charging was measured as 2.5×10^{13} m^{-2}. Since there was no noticeable change in the topography and roughness between the air condition and CP1, as well as between CP2 and CP3, we assumed ρ_{SSD} values for CP1 and CP2 the same as those for air and CP3, respectively. The density of GND is described by the Nix-Gao model [67] as follows:

$$\rho_{GND} = \frac{3}{2}\frac{1}{f^3}\frac{\tan^2\theta}{bh_f} \tag{15}$$

where θ is 19.7° in this study as the equivalent cone angle representing the angle between indenter and sample surface, b is the Burgers vector, h_f is the residual indentation depth, and f is the correction factor expressed as the ratio of the plastic zone radius to the contact area radius r_{pz}/r_c [70]. The r_c can be measured from the ECC images as shown in Fig. 8, while the r_{pz} can be estimated based on the Lawn's theory [71], which relies on the ratio of Young's modulus to the hardness E/H as follows:

$$r_{pz} = \varphi\left(\frac{E}{H}\right)^{\frac{1}{3}} tan^{\frac{1}{3}}(\theta) h_f \tag{16}$$

Here, φ is the geometry constant of 3.64 for the Berkovich indenter. The values of the relevant parameters under different conditions together with the physical meanings are summarized in Table 2. By considering the effect of hydrogen on lattice friction σ_H, the equation between the hardening behavior and indenting depth can be rearranged as follows:

$$P = CM\alpha\mu bA_c\sqrt{\rho_{SSD} + \frac{3}{2f^3}\frac{1\,tan^2\theta}{bh_f}} + C(\sigma_{Fric} + \sigma_H)A_c \tag{17}$$

By inserting the f factor calculated as 1.77 in the air condition, the curve obtained from Eq. (17) becomes fully consistent with the elastoplastic regime of the L-D curve obtained in air as shown in Fig. 11. The σ_H value in each cathodic polarization can be quantitatively obtained by fitting Eq. (17) with the elastoplastic part of the experimental L-D curves. Accordingly, the contribution of hydrogen to the lattice friction in the CoCrFeMnNi HEA is 95, 260, and 320 MPa at CP1, CP2, and CP3 polarizations, respectively. Such increases in the lattice friction are caused by the dissolved hydrogen atoms acting as the Cottrell atmosphere around moving dislocations [21]. This short-range interaction thus retards the dislocation motion and increases the hardness value.

Table 2

Parameters used for the elastoplastic regime fitting.

	Physical meaning	Air	CP1 (-1500 mV)	CP2 (-1600 mV)	CP3 (-1700 mV)
E (GPa)	Elastic modulus	201.4	202.8	201.2	184.4
H (GPa)	Hardness	3.36	3.77	4.67	5.21
h_f (nm)	Residual depth	115.2	105.7	90.8	82.7
r_{pz} (μm)	Plastic zone radius	1.17	1.03	0.82	0.70
r_c (μm)	Contact area radius	0.660	0.605	0.510	0.470
f	Correction factor	1.77	1.70	1.61	1.49
σ_H (MPa)	Hydrogen-enhanced lattice friction	0	95	260	320

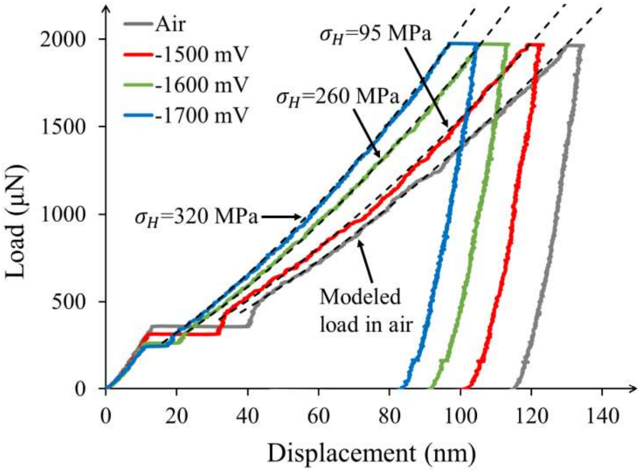

Fig. 11. The representative L-D curves for different conditions with the elastoplastic regime fitted by the Tabor relation-based Nix-Gao model.

5. Conclusion

A novel in-situ ECNI was used to examine the effects of hydrogen on the nanomechanical properties of a CoCrFeMnNi HEA. By applying cathodic charging at three different potentials and anodic discharging, the changes in the surface integrity, elastic modulus, pop-in load, and hardness were evaluated and analyzed. The main findings are summarized as follows.

1. There was no noticeable change on the sample surface during the cathodic charging process at -1500 mV, while irreversible slip lines accumulated as steps were detected at higher charging potentials of -1600 and -1700 mV. The formation of HISS is related to the plastic deformation caused by the hydrogen-induced internal stress and the intrinsic hydrogen effect on promoting dislocation nucleation through reducing the dislocation formation energy.

2. The HISS can irreversibly reduce the elastic modulus and the pop-in load. Specifically, the reduction of elastic modulus is caused by the increased surface roughness due to the HISS. The pop-in phenomenon in this circumstance is caused by the activation of pre-existing dislocation sources instead of homogeneous dislocation nucleation. The lower stress needed for activating the pre-existing dislocations and the stress concentration due to the increased surface roughness result in the reduced pop-in load.

3. The hardness is not influenced by the HISS and a reversible enhanced hardening behavior can be observed with the hydrogen ingress and egress processes. The enhanced hardness at cathodic charging conditions is related to the hydrogen-enhanced lattice friction due to the short-range interactions between dislocations and dissolved hydrogen.

4. To the best of our knowledge, the influences of HISS on the nanomechanical properties of materials especially on the studied alloy have not been discussed before. It will be necessary to consider this effect in future studies on hydrogen embrittlement and design of hydrogen-tolerant alloys.

Acknowledgements

The authors are grateful for the support provided by the Research Council of Norway through the HyF-Lex (244068/E30) project. The author (Dong Wang) would like to acknowledge the financial support from the China scholarship council.

Data availability

The raw/processed data required to reproduce these findings cannot be shared at this time as the data also forms part of an ongoing study.

Conflicts of interest

The authors declare no conflict of interest.

References:

[1] D.B. Miracle, O.N. Senkov, A critical review of high entropy alloys and related concepts, Acta Mater. 122 (2017) 448-511.

[2] J.W. Yeh, S.K. Chen, J.Y. Gan, S.J. Lin, T.S. Chin, T.T. Shun, C.H. Tsau, S.Y. Chang, Formation of simple crystal structures in Cu-Co-Ni-Cr-Al-Fe-Ti-V alloys with multiprincipal metallic elements, Metall. Mater. Trans. A 35a(8) (2004) 2533-2536.

[3] Z. Li, Interstitial equiatomic CoCrFeMnNi high-entropy alloys: carbon content, microstructure, and compositional homogeneity effects on deformation behavior, Acta Mater. 164 (2019) 400-412.

[4] T.K. Chen, T.T. Shun, J.W. Yeh, M.S. Wong, Nanostructured nitride films of multi-element high-entropy alloys by reactive DC sputtering, Surf. Coat. Technol. 188 (2004) 193-200.

[5] P.K. Huang, J.W. Yeh, T.T. Shun, S.K. Chen, Multi-principal-element alloys with improved oxidation and wear resistance for thermal spray coating, Adv. Eng. Mater. 6(1-2) (2004) 74-78.

[6] Y.F. Kao, S.K. Chen, J.H. Sheu, J.T. Lin, W.E. Lin, J.W. Yeh, S.J. Lin, T.H. Liou, C.W. Wang, Hydrogen storage properties of multi-principal-component CoFeMnTi(x)V(y)Zr(z) alloys, Int. J. Hydrog. Energy 35(17) (2010) 9046-9059.

[7] I.M. Robertson, P. Sofronis, A. Nagao, M.L. Martin, S. Wang, D.W. Gross, K.E. Nygren, Hydrogen Embrittlement Understood, Metall. Mater. Trans. A 46a(6) (2015) 2323-2341.

[8] H. Luo, Z.M. Li, A.M. Mingers, D. Raabe, Corrosion behavior of an equiatomic CoCrFeMnNi high-entropy alloy compared with 304 stainless steel in sulfuric acid solution, Corros. Sci. 134 (2018) 131-139.

[9] A.R. Troiano, R. Gibala, R. Hehemann, Hydrogen embrittlement and stress corrosion cracking: a Troiano Festschrift, ASM International, Ohio, 1984.

[10] W. Gerberich, 8 - Modeling hydrogen induced damage mechanisms in metals, in: R.P. Gangloff, B.P. Somerday (Eds.), Gaseous Hydrogen Embrittlement of Materials in Energy Technologies, Woodhead Publishing2012, pp. 209-246.

[11] D.P. Abraham, C.J. Altstetter, Hydrogen-enhanced localization of plasticity in an austenitic stainless steel, Metall. Mater. Trans. A 26(11) (1995) 2859-2871.

[12] P. Ferreira, I. Robertson, H. Birnbaum, Hydrogen effects on the interaction between dislocations, Acta Mater. 46(5) (1998) 1749-1757.

[13] S. Lynch, Hydrogen embrittlement phenomena and mechanisms, Corros. Rev. 30(3-4) (2012) 105-123.

[14] S.P. Lynch, Environmentally Assisted Cracking: Overview of Evidence for an Adsorption-Induced Localized-Slip Process, Acta Metall. 36(10) (1988) 2639-2661.

[15] R. Kirchheim, Reducing grain boundary, dislocation line and vacancy formation energies by solute segregation II. Experimental evidence and consequences, Acta Mater. 55(15) (2007) 5139-5148.

[16] R. Kirchheim, Reducing grain boundary, dislocation line and vacancy formation energies by solute segregation. I. Theoretical background, Acta Mater. 55(15) (2007) 5129-5138.

[17] R. Kirchheim, Revisiting hydrogen embrittlement models and hydrogen-induced homogeneous nucleation of dislocations, Scr. Mater. 62(2) (2010) 67-70.

[18] M. Koyama, E. Akiyama, K. Tsuzaki, Effect of hydrogen content on the embrittlement in a Fe-Mn-C twinning-induced plasticity steel, Corros. Sci. 59 (2012) 277-281.

[19] Z. Tarzimoghadam, M. Rohwerder, S.V. Merzlikin, A. Bashir, L. Yedra, S. Eswara, D. Ponge, D. Raabe, Multi-scale and spatially resolved hydrogen mapping in a Ni-Nb model alloy reveals the role of the δ phase in hydrogen embrittlement of alloy 718, Acta Mater. 109 (2016) 69-81.

[20] H. Luo, Z.M. Li, W.J. Lu, D. Ponge, D. Raabe, Hydrogen embrittlement of an interstitial equimolar high-entropy alloy, Corros. Sci. 136 (2018) 403-408.

[21] J. Song, W.A. Curtin, Mechanisms of hydrogen-enhanced localized plasticity: An atomistic study using alpha-Fe as a model system, Acta Mater. 68 (2014) 61-69.

[22] Y. Deng, A. Barnoush, Hydrogen embrittlement revealed via novel in situ fracture experiments using notched micro-cantilever specimens, Acta Mater. 142 (2018) 236-247.

[23] O. Barrera, D. Bombac, Y. Chen, T.D. Daff, E. Galindo-Nava, P. Gong, D. Haley, R. Horton, I. Katzarov, J.R. Kermode, C. Liverani, M. Stopher, F. Sweeney, Understanding and mitigating hydrogen embrittlement of steels: a review of experimental, modelling and design progress from atomistic to continuum, J. Mater. Sci. 53(9) (2018) 6251-6290.

[24] Z. Li, K.G. Pradeep, Y. Deng, D. Raabe, C.C. Tasan, Metastable high-entropy dual-phase alloys overcome the strength-ductility trade-off, Nature 534(7606) (2016) 227-30.

[25] A. Haglund, M. Koehler, D. Catoor, E.P. George, V. Keppens, Polycrystalline elastic moduli of a high-entropy alloy at cryogenic temperatures, Intermetallics 58 (2015) 62-64.

[26] H. Luo, Z. Li, D. Raabe, Hydrogen enhances strength and ductility of an equiatomic high-entropy alloy, Sci. Rep. 7(1) (2017) 9892.

[27] Y. Zhao, D.-H. Lee, M.-Y. Seok, J.-A. Lee, M.P. Phaniraj, J.-Y. Suh, H.-Y. Ha, J.-Y. Kim, U. Ramamurty, J.-i. Jang, Resistance of CoCrFeMnNi high-entropy alloy to gaseous hydrogen embrittlement, Scr. Mater. 135 (2017) 54-58.

[28] K.E. Nygren, K.M. Bertsch, S. Wang, H. Bei, A. Nagao, I.M. Robertson, Hydrogen embrittlement in compositionally complex FeNiCoCrMn FCC solid solution alloy, Curr. Opin. Solid State Mater. Sci. 22(1) (2018) 1-7.

[29] Y. Zhao, D.-H. Lee, J.-A. Lee, W.-J. Kim, H.N. Han, U. Ramamurty, J.-Y. Suh, J.-i. Jang, Hydrogen-induced nanohardness variations in a CoCrFeMnNi high-entropy alloy, Int. J. Hydrog. Energy 42(16) (2017) 12015-12021.

[30] A. Barnoush, H. Vehoff, Electrochemical nanoindentation: A new approach to probe hydrogen/deformation interaction, Scr. Mater. 55(2) (2006) 195-198.

[31] A. Barnoush, Correlation between dislocation density and nanomechanical response during nanoindentation, Acta Mater. 60(3) (2012) 1268-1277.

[32] D. Wang, X. Lu, Y. Deng, X. Guo, A. Barnoush, Effect of hydrogen on nanomechanical properties in Fe-22Mn-0.6C TWIP steel revealed by in-situ electrochemical nanoindentation, Acta Mater. 166 (2019) 618-629.

[33] M. Asgari, A. Barnoush, R. Johnsen, R. Hoel, Nanomechanical evaluation of the protectiveness of nitrided layers against hydrogen embrittlement, Corros. Sci. 62 (2012) 51-60.

[34] X. Lu, Y. Ma, M. Zamanzade, Y. Deng, D. Wang, W. Bleck, W.W. Song, A. Barnoush, Insight into hydrogen effect on a duplex medium-Mn steel revealed by in-situ nanoindentation test, Int. J. Hydrog. Energy 44(36) (2019) 20545-20551.

[35] M. Kappes, G.S. Frankel, R. Thodla, M. Mueller, N. Sridhar, R.M. Carranza, Hydrogen Permeation and Corrosion Fatigue Crack Growth Rates of X65 Pipeline Steel Exposed to Acid Brines Containing Thiosulfate or Hydrogen Sulfide, Corrosion 68(11) (2012).

[36] X. Lu, D. Wang, Z. Li, Y. Deng, A. Barnoush, Hydrogen susceptibility of an interstitial equimolar high-entropy alloy revealed by in-situ electrochemical microcantilever bending test, Mater. Sci. Eng. A 762 (2019) 138114.

[37] I. Gutierrez-Urrutia, D. Raabe, Dislocation and twin substructure evolution during strain hardening of an Fe-22 wt.% Mn-0.6 wt.% C TWIP steel observed by electron channeling contrast imaging, Acta Mater. 59(16) (2011) 6449-6462.

[38] S. Zaefferer, N.N. Elhami, Theory and application of electron channelling contrast imaging under controlled diffraction conditions, Acta Mater. 75 (2014) 20-50.

[39] K.L. Johnson, Contact Mechanics, Cambridge University Press, Cambridge, 1987.

[40] S.F. Liu, Y. Wu, H.T. Wang, J.Y. He, J.B. Liu, C.X. Chen, X.J. Liu, H. Wang, Z.P. Lu, Stacking fault energy of face-centered-cubic high entropy alloys, Intermetallics 93 (2018) 269-273.

[41] A. Barnoush, H. Vehoff, Recent developments in the study of hydrogen embrittlement: Hydrogen effect on dislocation nucleation, Acta Mater. 58(16) (2010) 5274-5285.

[42] W.W. Gerberich, J.C. Nelson, E.T. Lilleodden, P. Anderson, J.T. Wyrobek, Indentation induced dislocation nucleation: The initial yield point, Acta Mater. 44(9) (1996) 3585-3598.

[43] W.C. Oliver, G.M. Pharr, Measurement of hardness and elastic modulus by instrumented indentation: Advances in understanding and refinements to methodology, J. Mater. Res. 19(1) (2004) 3-20.

[44] A.E. Pontini, J.D. Hermida, X-ray diffraction measurement of the stacking fault energy reduction induced by hydrogen in an AISI 304 steel, Scr. Mater. 37(11) (1997) 1831-1837.
[45] V. Olden, C. Thaulow, R. Johnsen, Modelling of hydrogen diffusion and hydrogen induced cracking in supermartensitic and duplex stainless steels, Mater. Des. 29(10) (2008) 1934-1948.
[46] H.K. Birnbaum, P. Sofronis, Hydrogen-enhanced localized plasticity—a mechanism for hydrogen-related fracture, Mater. Sci. Eng. A 176(1) (1994) 191-202.
[47] M. Hoelzel, S.A. Danilkin, H. Ehrenberg, D.M. Toebbens, T.J. Udovic, H. Fuess, H. Wipf, Effects of high-pressure hydrogen charging on the structure of austenitic stainless steels, Mater. Sci. Eng. A 384(1-2) (2004) 255-261.
[48] D.G. Ulmer, C.J. Altstetter, Phase-Relations in the Hydrogen Austenite System, Acta Metall. Mater. 41(7) (1993) 2235-2241.
[49] G. Laplanche, P. Gadaud, O. Horst, F. Otto, G. Eggeler, E.P. George, Temperature dependencies of the elastic moduli and thermal expansion coefficient of an equiatomic, single-phase CoCrFeMnNi high-entropy alloy, J. Alloys Compd. 623 (2015) 348-353.
[50] Z. Wu, C.M. Parish, H. Bei, Nano-twin mediated plasticity in carbon-containing FeNiCoCrMn high entropy alloys, J. Alloys Compd. 647 (2015) 815-822.
[51] A.J. Zaddach, C. Niu, C.C. Koch, D.L. Irving, Mechanical Properties and Stacking Fault Energies of NiFeCrCoMn High-Entropy Alloy, Jom 65(12) (2013) 1780-1789.
[52] K. Tomatsu, K. Miyata, T. Omura, Electrochemical Nanoindentation Study on Influence of Hydrogen on Local Mechanical Properties of Fcc Metals at Slow Strain Rate, ISIJ Int. 56(3) (2016) 418-423.
[53] V.R. Skalskyi, Z.T. Nazarchuk, S.I. Hirnyi, Effect of electrolytically absorbed hydrogen on Young's modulus of structural steel, Materials Science 48(4) (2013) 491-499.
[54] E. Lunarska, A. Zielinski, M. Smialowski, Effect of Hydrogen on Shear Modulus of Polycrystalline Alpha-Iron, Acta Metall. 25(3) (1977) 305-308.
[55] W.G. Jiang, J.J. Su, X.Q. Feng, Effect of surface roughness on nanoindentation test of thin films, Eng. Fract. Mech. 75(17) (2008) 4965-4972.
[56] C. Begau, A. Hartmaier, E.P. George, G.M. Pharr, Atomistic processes of dislocation generation and plastic deformation during nanoindentation, Acta Mater. 59(3) (2011) 934-942.
[57] J. Frenkel, Zur Theorie der Elastizitätsgrenze und der Festigkeit kristallinischer Körper, 37(7) (1926) 572-609.
[58] P.M. Anderson, J.P. Hirth, J. Lothe, Theory of Dislocations, 3rd ed., Cambridge University Press, Cambridge, 2017.
[59] I.M. Robertson, The effect of hydrogen on dislocation dynamics, Eng. Fract. Mech. 68(6) (2001) 671-692.
[60] A. Barnoush, H. Vehoff, Hydrogen embrittlement of aluminum in aqueous environments examined by in situ electrochemical nanoindentation, Scr. Mater. 58(9) (2008) 747-750.
[61] M. Zamanzade, H. Vehoff, A. Barnoush, Cr effect on hydrogen embrittlement of Fe3Al-based iron aluminide intermetallics: Surface or bulk effect, Acta Mater. 69 (2014) 210-223.
[62] M.Q. Chandler, M.F. Horstemeyer, M.I. Baskes, P.M. Gullett, G.J. Wagner, B. Jelinek, Hydrogen effects on nanovoid nucleation in face-centered cubic single-crystals, Acta Mater. 56(1) (2008) 95-104.
[63] P.J. Ferreira, I.M. Robertson, H.K. Birnbaum, Influence of hydrogen on the stacking-fault energy of an austenitic stainless steel, Mater. Sci. Forum 207-209 (1996) 93-96.
[64] A. Bamoush, N. Kheradmand, T. Hajilou, Correlation between the hydrogen chemical potential and pop-in load during in situ electrochemical nanoindentation, Scr. Mater. 108 (2015) 76-79.
[65] D.B. Shan, L. Yuan, B. Guo, Multiscale simulation of surface step effects on nanoindentation, Mater. Sci. Eng. A 412(1-2) (2005) 264-270.
[66] Z.G. Wang, H. Bei, E.P. George, G.M. Pharr, Influences of surface preparation on nanoindentation pop-in in single-crystal Mo, Scr. Mater. 65(6) (2011) 469-472.
[67] W.D. Nix, H.J. Gao, Indentation size effects in crystalline materials: A law for strain gradient plasticity, J. Mech. Phys. Solids 46(3) (1998) 411-425.

[68] J.Y. He, H. Wang, H.L. Huang, X.D. Xu, M.W. Chen, Y. Wu, X.J. Liu, T.G. Nieh, K. An, Z.P. Lu, A precipitation-hardened high-entropy alloy with outstanding tensile properties, Acta Mater. 102 (2016) 187-196.
[69] O. Bouaziz, S. Allain, C.P. Scott, P. Cugy, D. Barbier, High manganese austenitic twinning induced plasticity steels: A review of the microstructure properties relationships, Curr. Opin. Solid State Mater. Sci. 15(4) (2011) 141-168.
[70] K. Durst, B. Backes, M. Goken, Indentation size effect in metallic materials: Correcting for the size of the plastic zone, Scr. Mater. 52(11) (2005) 1093-1097.
[71] B.R. Lawn, A.G. Evans, D.B. Marshall, Elastic/Plastic Indentation Damage in Ceramics: The Median/Radial Crack System, J. Am. Ceram. Soc. 63(9-10) (1980) 574-581.

Conflicts of interest

The authors declare no conflict of interest.